

UCLA

UCLA Previously Published Works

Title

The tides of Mercury and possible implications for its interior structure

Permalink

<https://escholarship.org/uc/item/2z40c3sn>

Authors

Padovan, Sebastiano
Margot, Jean-Luc
Hauck, Steven A
[et al.](#)

Publication Date

2014

DOI

10.1002/2013JE004459

Peer reviewed

The tides of Mercury and possible implications for its interior structure

Sebastiano Padovan¹, Jean-Luc Margot^{1,2}, Steven A. Hauck, II³, William B. Moore^{4,5}, and Sean C. Solomon^{6,7}

¹Department of Earth, Planetary, and Space Sciences, University of California, Los Angeles, California, USA.

²Department of Physics and Astronomy, University of California, Los Angeles, California, USA.

³Department of Earth, Environmental, and Planetary Sciences, Case Western University, Cleveland, Ohio, USA.

⁴Department of Atmospheric and Planetary Sciences, Hampton University, Virginia, USA.

⁵National Institute of Aerospace, Hampton, Virginia, USA.

⁶Lamont-Doherty Earth Observatory, Columbia University, Palisades, New York, USA.

⁷Department of Terrestrial Magnetism, Carnegie Institution of Washington, Washington, D.C., USA.

Abstract

The combination of the radio tracking of the MESSENGER spacecraft and Earth-based radar measurements of the planet's spin state gives three fundamental quantities for the determination of the interior structure of Mercury: mean density ρ , moment of inertia C , and moment of inertia of the outer solid shell C_m . This work focuses on the additional information that can be gained by a determination of the change in gravitational potential due to planetary tides, as parametrized by the tidal potential Love number k_2 . We investigate the tidal response for sets of interior models that are compatible with the available constraints (ρ , C , and C_m). We show that the tidal response correlates with the size of the liquid core and the mean density of material below the outer solid shell, and that it is affected by the rheology of the outer solid shell of the planet, which depends on its temperature and mineralogy. For a mantle grain size of 1 cm, we calculate that the tidal k_2 of Mercury is in the range 0.45 to 0.52. Some of the current models for the interior structure of Mercury are compatible with the existence of a solid FeS layer at the top of the core. Such a layer, if present, would increase the tidal response of the planet.

1 Introduction

In the absence of an in situ geophysical network, what we know of the interior of Mercury is based on a combination of Earth-based observations, spacecraft exploration, and theoretical insight. Earth-based radar observations provide measurements of the obliquity of Mercury and the amplitude of

its forced libration (*Margot et al.*, 2007, 2012). Through radio tracking of the MErcury Surface, Space ENvironment, GEochemistry, and Ranging (MESSENGER) spacecraft, the gravitational field of the planet has been determined (*Smith et al.*, 2012). Given that Mercury is in a Cassini state (*Colombo*, 1966; *Peale*, 1969), the spin parameters (obliquity θ and angle of libration γ), when combined with the second harmonic degree components of the gravity field (J_2 and C_{22}), provide two important integral constraints for the interior of Mercury, the moment of inertia C (*Peale*, 1969) and, in the presence of a global liquid layer, the moment of inertia of the outer solid shell C_m (*Peale*, 1976). These two moments, along with the mean density ρ , are three constraints that any model of the interior of Mercury must satisfy (*Hauck et al.*, 2013).

The measurement of the deformation of a planet due to periodic tidal forcing can be used to place additional bounds on the interior structure, because the tidal response is a function of the density, rigidity, and viscosity of the subsurface materials. This property has been applied in the past to support the hypothesis of a liquid core in Venus (*Konopliv and Yoder*, 1996) and a global liquid ocean in Titan (*Iess et al.*, 2012). *Yoder et al.* (2003) used the measurement of the tides to reveal the liquid state of the Martian core and to estimate its radius. It is interesting to note that the interior structures of Venus and Mars are currently less well-characterized than that of Mercury, since for Mars the moment of inertia of the outer solid shell is not known, and for Venus only the mean density and k_2 tidal deformation are known, but no moment of inertia information is available.

The motivation for this paper is to explore the information that can be gained about the interior of Mercury by the combination of the determinations of ρ , C , and C_m with the measurement of k_2 , which will indicate the 88-day annual tidal k_2 .

We model the tidal response of Mercury for a range of interior structures that are compatible with the mean density ρ and the moments of inertia C and C_m (*Hauck et al.*, 2013). The formalism that we employ is described in section 2, and section 3 describes the interior models that we use and the assumptions that we make in the evaluation of the tidal response. The rheology of the outer solid shell is discussed in section 4. The results of our simulations are presented in section 5 (the minor effects of the properties of the inner core on the tidal response are explored in Appendix A). We discuss the implications of the detection of the tidal response for the physical characterization of the interior of Mercury in section 6.

2 Planetary Tidal Deformation

Mercury’s solar tides are caused by the difference in the gravitational attraction of the Sun across the planet. Denoting the mass of the Sun by M_S , the expression for the solar tide-generating potential Φ at a point P inside the planet is

$$\Phi = \frac{GM_S}{d} = \frac{GM_S}{r_S} \left[\sum_{n=2}^{\infty} \left(\frac{r'}{r_S} \right)^n P_n(\cos \psi_P) \right] = \sum_{n=2}^{\infty} \Phi_n, \quad (1)$$

where the summation follows from the expansion for $(1/d)$, and d is the distance between P and the Sun (e.g., *Arfken and Weber*, 2005). The angle ψ_P is the angle between r' and r_S , the distances from the center of mass of the body to P and to the Sun, respectively. P_n indicates the

Legendre polynomial of degree n . G is the gravitational constant. We introduce Φ_n to highlight the dependence of Φ on the n^{th} power of the factor $(r'/r_S) \ll 1$. For a point on the surface, we set $r' = R_M$, the radius of Mercury, and r_S equal to a_M , the semimajor axis of Mercury's orbit, and we can express the largest component of the potential as $g\zeta P_2(\cos \psi_P)$, where $g = (GM_M/R_M^2)$ is the gravitational acceleration at the surface, M_M is the mass of Mercury, $\zeta P_2(\cos \psi_P)$ is the height of the equilibrium tide (*Murray and Dermott, 1999*), and where

$$\zeta = \frac{M_S}{M_M} \left(\frac{R_M}{a_M} \right)^3 R_M. \quad (2)$$

Among the terrestrial planets ζ is the largest for Mercury, with a value of ~ 1.10 m (for comparison $\zeta_{\text{Venus}} \sim 0.43$ m, $\zeta_{\text{Earth}} \sim 0.16$ m, and $\zeta_{\text{Mars}} \sim 0.03$ m).

The harmonic expansion of the tide-generating potential in equation (1) can be used to identify all the different tidal components (in period and amplitude) generated by the Sun at Mercury (*Van Hoolst and Jacobs, 2003*). The largest component has a timescale equal to the orbital period of Mercury around the Sun (~ 88 days). This annual tidal perturbation periodically modifies the shape of Mercury, and thus the distribution of matter inside the planet, with an accompanying modification of its gravitational field. This modification is parameterized with the potential Love number k_2 , which relates the additional potential ϕ_{2t} due to the deformation of the planet to the tide-generating potential Φ_2 due to the Sun:

$$\phi_{2t} = k_2(\omega) \Phi_2. \quad (3)$$

The subscript 2 indicates that the main deformation is generated by the largest term of the expansion, which corresponds to $n = 2$. The frequency ω indicates that the response of the body, described by k_2 , depends on the period (i.e., frequency) of the applied forcing, which for the case considered here is the 88-day-period solar tide.

The study of the deformation of a planet under the perturbation of an external potential requires the solution of the equations of motion inside the body. Using a spherical harmonic decomposition in latitude and longitude, we transform these three second-order ordinary differential equations into six first-order linear differential equations in radius (*Alterman et al., 1959*). The motion is controlled both by material stresses (elastic or viscoelastic) and gravitational forces, the latter originating from a gravitational potential that is the sum of the self-gravitation of the planet and the external tidal potential. The framework for the solution is formally the same both for elastic rheologies and for viscoelastic rheologies, thanks to the correspondence principle (*Biot, 1954*). The results presented in the following sections are obtained by modeling Mercury as a series of homogeneous incompressible layers. Each layer is characterized by thickness, density, rigidity, and viscosity (*Wolf, 1994*). In evaluating the tidal response, we use the formalism developed by *Moore and Schubert (2000)*.

The possible values for the k_2 of a planet range between 0 for a perfectly rigid body that does not deform, and 1.5, the value for a homogeneous fluid body (for these idealized bodies the limits are independent of the forcing frequency). Values for k_2 have been determined for Venus (*Konopliv and Yoder, 1996*), the Moon (*Konopliv et al., 2013; Lemoine et al., 2013*), Mars (*Konopliv et al., 2011*), and Titan (*Iess et al., 2012*). The k_2 of the Moon is uncertain at the $\sim 0.5\%$ level, a result

of the high-quality data obtained with the Gravity Recovery and Interior Laboratory (GRAIL) mission (*Zuber et al.*, 2013). For Mars the estimate is uncertain at the $\sim 5\%$ level, a result obtained by combining data from a large number of spacecraft missions, including a lander and two years of tracking data from the low-altitude, nearly circular orbital phase of the Mars Reconnaissance Orbiter. For Venus and Titan the estimates have an uncertainty $\gtrsim 10\%$. A numerical simulation of the determination of Mercury’s k_2 with BepiColombo, the future dual orbiter mission to Mercury by the European Space Agency and the Japan Aerospace Exploration Agency, indicates an expected accuracy of $\sim 1\%$ (*Milani et al.*, 2001). This figure represents a lower bound for MESSENGER, because its eccentric orbit makes the detection of k_2 more challenging. The uncertainty on the determination of the k_2 of Mercury as obtained from MESSENGER is expected to be $\sim 10\%$ (*Mazarico et al.*, 2014).

2.1 Rheological Models of the Interior

The mantle of Earth responds elastically on the short timescales associated with the waves generated by earthquakes but flows like a fluid on the geologically long timescales of mantle convection. The Maxwell rheological model is the simplest model that captures this short- and long-timescale behavior. It is completely defined by two parameters, the unrelaxed (infinite-frequency) rigidity μ_U and the dynamic viscosity ν . The Maxwell time, defined as

$$\tau_M = \frac{\nu}{\mu_U}, \quad (4)$$

is a timescale that separates the elastic regime (forcing period $\ll \tau_M$) from the fluid regime (forcing period $\gg \tau_M$). This simple rheological model is sufficiently accurate for the crust, which is cold and responds elastically, and the liquid core, which has zero rigidity and therefore a fluid response. The inner core, if present, has a negligible effect on the tidal response (Appendix A), so for simplicity we use a Maxwell model to describe its rheology. Nevertheless the Maxwell model does not provide a good fit to laboratory and field data in the low-frequency seismological range, and thus it should not be used to model the response of the mantle at tidal frequencies (e.g., *Efroimsky and Lainey*, 2007; *Nimmo et al.*, 2012).

Jackson et al. (2010) explored three different parameterizations (Burgers, extended Burgers, and Andrade pseudo-period) to fit torsional oscillation data from a set of melt-free olivine samples. Both the Burgers models and the Andrade model provide a good fit for the low-frequency data. The small number of parameters required for the Andrade model makes it more attractive to model the rheology of Mercury, for which we lack any ground-truth data. Note, however, that both the Burgers models and the Andrade model have not been tested at periods longer than 10^3 s, so when applied to the study of planetary tidal deformation (period $> 10^6$ s) they both need to be extrapolated (for an application of the extended Burgers model to the mantle of the Moon and Mars see *Nimmo et al.* (2012) and *Nimmo and Faul* (2013), respectively).

We report here the expressions for the real and imaginary part of the dynamic compliance $J(\omega)$

for the Andrade-pseudoperiod model, as described by *Jackson et al.* (2010):

$$J_{\text{R}}(\omega) = \frac{1}{\mu_{\text{U}}} \left\{ 1 + \beta^* \Gamma(1+n) \omega^{-n} \cos\left(\frac{n\pi}{2}\right) \right\}, \quad (5)$$

$$J_{\text{I}}(\omega) = \frac{1}{\mu_{\text{U}}} \left\{ \beta^* \Gamma(1+n) \omega^{-n} \sin\left(\frac{n\pi}{2}\right) + \frac{1}{\omega \tau_{\text{M}}} \right\} \quad (6)$$

The unrelaxed rigidity is μ_{U} and $\beta^* = \beta \mu_{\text{U}}$. The coefficient β , along with n , appear in the expression of the Andrade creep $J(t) = 1/\mu_{\text{U}} + \beta t^n + t/\nu$, where Γ is the gamma function and τ_{M} the Maxwell time. The frequency ω is obtained from $\omega = 2\pi/X_{\text{B}}$, where X_{B} is the pseudo-period master variable introduced by *Jackson et al.* (2010):

$$X_{\text{B}} = T_0 \left(\frac{d}{d_{\text{R}}} \right)^{-m} \exp \left[\left(\frac{-E_{\text{B}}}{R} \right) \left(\frac{1}{T} - \frac{1}{T_{\text{R}}} \right) \right] \exp \left[\left(\frac{-V}{R} \right) \left(\frac{P}{T} - \frac{P_{\text{R}}}{T_{\text{R}}} \right) \right], \quad (7)$$

which takes into account the effects of pressure P , temperature T , and grain-size d . The subscript R indicates reference value. T_0 is the forcing period (for Mercury ~ 88 days). The exponent m characterizes the dependence on the grain size, which in principle can be different for anelastic processes (m_a) and for viscous relaxation (m_v). We tested that at the frequency of the Mercury tide, the effect is minor, and we assumed $m_a = m_v = m$. The other quantities are defined in Table 1. The dynamic compliance was evaluated by setting the value of τ_{M} in equation (6) equal to the reference value reported by *Jackson et al.* (2010, Table 2, $\tau_{\text{MR}} = 10^{5.3}$ s), and including the effects of T , P , and d through the pseudo-period master variable defined in equation (7). The dynamic compliance is related to the inverse quality factor Q^{-1} and the rigidity μ by

$$Q^{-1}(\omega) = \frac{J_{\text{I}}(\omega)}{J_{\text{R}}(\omega)}, \quad (8)$$

$$\mu(\omega) = [J_{\text{R}}^2(\omega) + J_{\text{I}}^2(\omega)]^{-1/2}. \quad (9)$$

To illustrate the importance of choosing a realistic rheological model, in Figure 1 we show how the rigidity of a material with $\mu_{\text{U}} = 65$ GPa varies as a function of the forcing frequency for two temperatures, at a pressure of 5.5 GPa, representative of conditions at the base of the mantle of Mercury (*Hauck et al.*, 2013). Both the Maxwell rheological model and the Andrade model are plotted. They both predict a fluid response (i.e., zero rigidity) at high temperatures and/or long forcing frequencies, but the Maxwell model underestimates non-elastic effects at forcing periods that are shorter than the Maxwell time. This effect is particularly relevant for Mercury, for which the core-mantle boundary temperature may be above 1600 K (*Rivoldini and Van Hoolst*, 2013; *Tosi et al.*, 2013).

3 Methods

Throughout this work (except section 3.1) we use models compatible with the available constraints, i.e., mean density ρ , moment of inertia C , and moment of inertia of the solid outer shell C_m

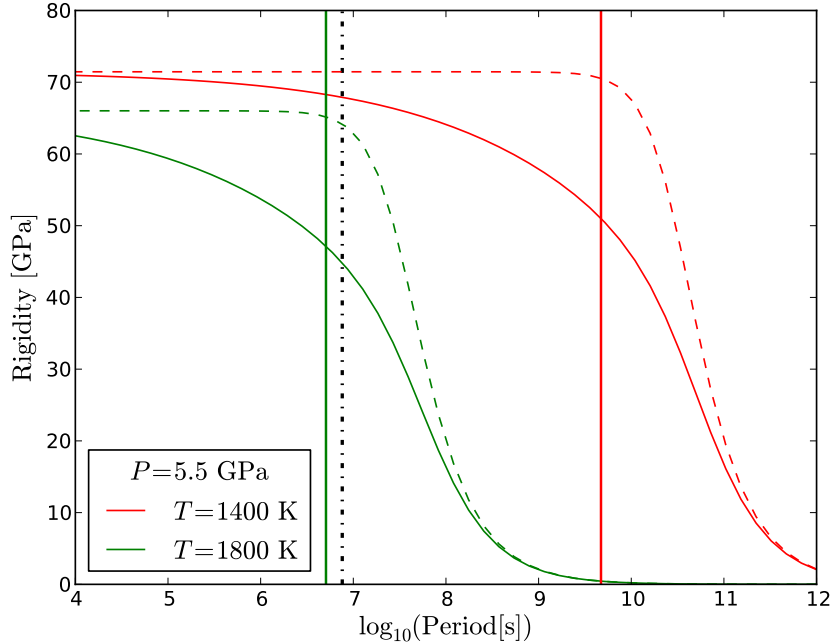


Figure 1: Comparison of the Andrade (solid lines) and Maxwell (dashed lines) rheological models at a pressure of 5.5 GPa for two different temperatures, $T = 1400$ K (red) and $T = 1800$ K (green). The solid colored vertical lines represent the Maxwell times. The dash-dotted line indicates the forcing frequency of Mercury’s tide. Note that at $T = 1800$ K the Maxwell model over-estimates the rigidity at the tidal frequency by about 35% compared with the Andrade model. The unrelaxed modulus used in these example is 65 GPa.

(section 1). By compatible we mean that the distributions of ρ , C , and C_m in the set of interior models considered here are approximately Gaussian with means and standard deviations that match the nominal values of the observables and their one-standard-deviation errors. The mean density ρ has a Gaussian distribution with mean and standard deviation equal to 5430 kg/m^3 and 10 kg/m^3 , respectively. For C and C_m , we choose Gaussian distributions with means and standard deviations defined by the observed values and errors reported by *Margot et al.* (2012). Accordingly $C/M_M R_M^2 = 0.346 \pm 0.014$ and $C_m/C = 0.431 \pm 0.025$ (*Margot et al.*, 2012).

The small abundance of Fe and relatively large abundance of S at the surface of Mercury imply strongly reducing conditions within the planet (*Nittler et al.*, 2011). Under these conditions both silicon and sulfur likely partitioned into the core during Mercury’s formation and differentiation (*Hauck et al.*, 2013). Of the five compositional models for the interior of Mercury analyzed by *Hauck et al.* (2013), we focus on two sets that have a Si-bearing core, because they are consistent with the inferred reducing conditions. The major difference between the two sets is the presence or absence of a solid FeS layer at the top of the core. We label these two sets the FeS-set and NoFeS-set, respectively.

Table 1: Rheological Models for the Interior of Mercury^a.

Layer	Model	Parameter	Definition	Value	Notes
Crust	Maxwell				Section 4.3
		μ_U	Unrelaxed rigidity	55 GPa	
		ν	Dynamic viscosity	10^{23} Pa s	
Mantle	Andrade ^b				Section 2.1
		μ_U	Unrelaxed rigidity	59 – 71 GPa	Section 4.2
		T_b	Mantle basal temperature ^c	1600 – 1850 K	Section 3.2
		n	Andrade creep coefficient	0.3	
		β^*	Andrade creep parameter	0.02	
		P_R	Reference pressure	0.2 GPa	
		T_R	Reference temperature	1173 K	
		d_R	Reference grain-size	3.1 μm	
		d	Grain size	1mm – 1cm	
		m	Grain size exponent	1.31	
		V	Activation volume	10^{-5} m ³ mol ⁻¹	
		E_B	Activation energy	303×10^3 kJ mol ⁻¹	
FeS	Andrade ^d				Section 4.4
Outer core	Maxwell				Section 2.1
		μ_U	Unrelaxed rigidity	0 GPa	
		ν	Dynamic viscosity	0 Pa s	
Inner core	Maxwell				Appendix A
		μ_U	Unrelaxed rigidity	10^{11} GPa	
		ν	Dynamic viscosity	10^{20} Pa s	

^a The models are introduced in Section 2.1

^b The fixed parameters of the Andrade model are based on the results of *Jackson et al.* (2010).

^c Here we report T_b because the temperature T in equation (7) depends on the temperature profile, which is controlled by T_b .

^d The FeS layer is assumed to have the same rheology as that of the base of the mantle.

The possible presence of an FeS layer was initially predicated on the basis of the inferred highly reducing conditions and the then-best estimate of the high mean density of the outer solid shell (*Smith et al.*, 2012). Improved values of the obliquity θ (*Margot et al.*, 2012) led to a revised value for the mean density of the outer solid shell (*Hauck et al.*, 2013) and made the density argument for the presence of the FeS layer less compelling. Nevertheless, the geochemical argument supporting the presence of the FeS layer is still valid (*Hauck et al.*, 2013), and a conductive layer above the convective liquid core is one of the possible explanations for Mercury’s weak magnetic field (*Christensen*, 2006; *Anderson et al.*, 2012).

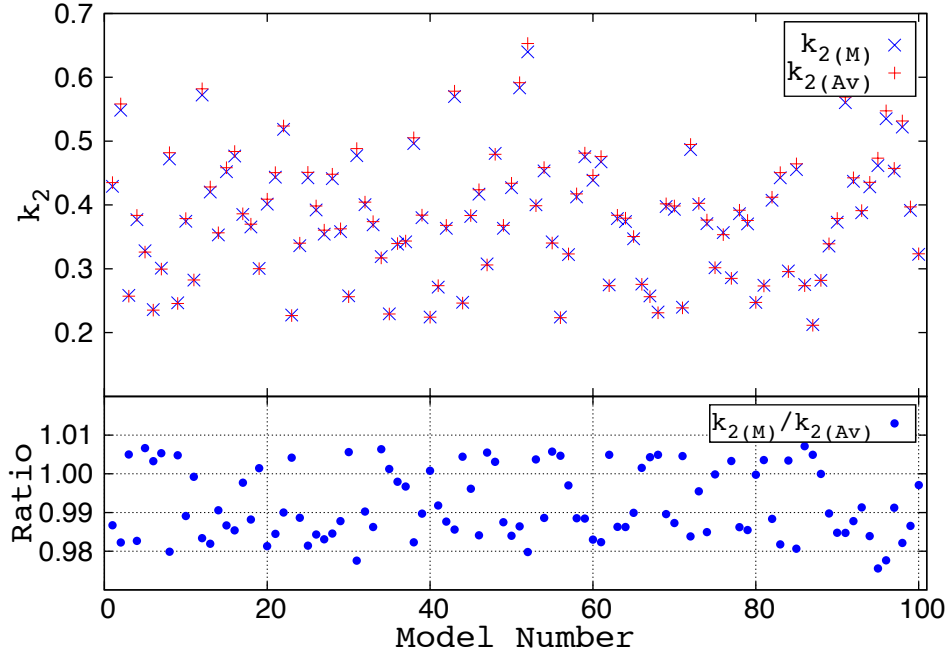


Figure 2: Effect of the radial density profile on the magnitude of k_2 . For each of a set of 100 models, the value of k_2 has been calculated both for the ~ 1000 -layer version ($k_{2(M)}$) and for the 5-layer version ($k_{2(Av)}$). (Bottom) The ratio of the two determinations, which in most cases is within 2% of unity. The models used for this plot are constrained only by the mean density of Mercury.

3.1 Radial Density Profile

The radial density profiles that we used as input (*Hauck et al.*, 2013) are given as series of constant-property layers, going from the center to the surface. The crust, mantle, and FeS layer are modeled as constant-density shells. This simplification is justified by the small thickness of the outer solid shell of Mercury and by the relatively low surface gravitational acceleration but does not affect the characterization of the interior of the planet on the basis of the measured values of ρ , C , and C_m (*Hauck et al.*, 2013). The core (inner+outer) is represented with ~ 1000 layers in order to take into account the effects of self-compression and temperature in the equation of state for core materials, as was done by *Hauck et al.* (2013). However, the Love number k_2 is a global parameter, summarizing the response of the planet to tidal forcing, and it is not very sensitive to the fine density structure. We verified that k_2 calculations can be performed accurately with simplified, 4- or 5-layer models instead of the original ~ 1000 -layer models. In order to establish this point, we used a random sample of 100 models drawn from the FeS-set and constrained only by the mean density ρ of Mercury. For this test we did not apply the moment of inertia constraints (C and C_m), as this allowed us to explore a larger parameter space and resulted in a more robust test. For each one of the 100 models we computed an averaged version, characterized by five constant-density layers. Computed k_2 values for the ~ 1000 -layer models and the corresponding 5-layer models are shown in the top panel of Figure 2. Their ratio (Figure 2, bottom panel) indicates that errors introduced by using the simplified models are $\lesssim 2\%$. In view of this result and of the $\sim 10\%$

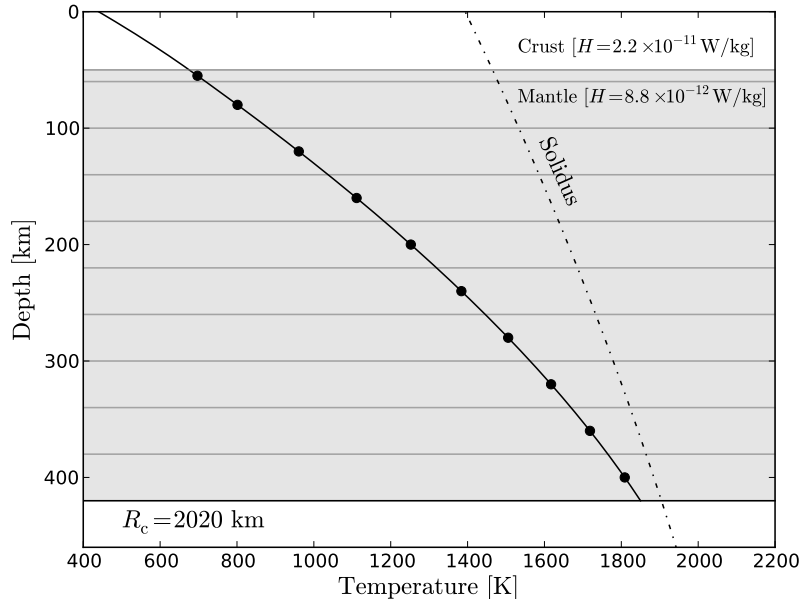


Figure 3: Temperature (solid line) as a function of depth for a model with a 2020-km radius core and a 50-km-thick crust. The values for the heat production rate in the crust and mantle are indicated. The dots represent the midpoint of each mantle sublayer, for which the temperature and pressure are used to derive a rheology for the sublayer. The peridotite solidus of *Hirschmann* (2000) is also shown.

expected accuracy of MESSENGER’s k_2 determination (section 2), in what follows we show results obtained with the simplified 4- or 5-layer models. This approach reduces the computational cost by \sim three orders of magnitude.

3.2 Pressure and Temperature Profiles in the Mantle

To calculate a rheological profile for the mantle of Mercury with the Andrade rheological model described in Section 2.1, the pressure and temperature as a function of depth must be calculated.

At the radius r in the mantle the pressure is simply obtained as an overburden load $P(r) = g[\rho_c h_c + \rho_m h_m(r)]$, where the subscripts “c” and “m” refer to the crust and mantle, respectively. h_c is the crustal thickness, and $h_m(r)$ is the thickness of the mantle above r (i.e., $r + h_m(r) + h_c = R_M$).

We obtained the temperature profile by solving the static heat conduction equation with heat sources in spherical coordinates (e.g., *Turcotte and Schubert, 2002*) in the mantle and crust:

$$k \frac{1}{r^2} \frac{d}{dr} \left(r^2 \frac{dT}{dr} \right) + \rho H = 0. \quad (10)$$

In equation (10) k is the thermal conductivity, ρ is the density, and H is the heat production rate.

We assumed a homogeneous distribution of heat sources in the crust and in the mantle. The distribution in the crust might be exponential as in the crust of the Earth, but we verified that this would only marginally affect the deep-mantle temperature profile. The value of H at the surface, H_0 , has been inferred from MESSENGER measurements and is equal to $H_0 = 2.2 \times 10^{-11} \text{ W kg}^{-1}$ (Peplowski *et al.*, 2011). We adopted the surface value H_0 for the heat production rate in the crust, $H_c = H_0$. For the distribution of heat sources in the mantle we used $H_m = H_0/2.5$, which is compatible with the enrichment factor derived by Tosi *et al.* (2013). The value of k is set to $3.3 \text{ Wm}^{-1}\text{K}^{-1}$.

As boundary conditions we applied the surface temperature T_s and the temperature at the base of the mantle T_b . T_s is set to 440 K, a value obtained with a simple equilibrium temperature calculation. Therefore in our models the temperature profile is controlled by the temperature T_b . There are currently few constraints on T_b , but two independent sets of workers (Rivoldini and Van Hoolst, 2013; Tosi *et al.*, 2013) point to the range 1600-1900 K. We defined two end-members profiles: a cold mantle with $T_b = 1600 \text{ K}$, and a hot mantle with $T_b = 1850 \text{ K}$. We consider $T_b = 1850 \text{ K}$ as our hot mantle case, since, from the peridotite solidus of Hirschmann (2000), $T_b = 1900 \text{ K}$ would result in partial melting at the base of the mantle (Figure 3). We did not consider in this work the presence of partial melting.

The rheological models described in section 2.1 strongly depend on the temperature. Our end-member temperature profiles are obtained under the assumption of a conductive mantle. This assumption is consistent with the results of Tosi *et al.* (2013), which indicate that the mantle of Mercury is most likely conductive at the present time. Nevertheless, a present-day convective mantle is not excluded (Michel *et al.*, 2013; Tosi *et al.*, 2013). A convective mantle for the $T_b = 1850 \text{ K}$ case would result in partial melting (Figure 3). A convective profile with $T_b = 1600 \text{ K}$ would be more dissipative and deformable than the conductive case (since in the convective envelope the temperature is approximately constant and equal to T_b), but this effect is similar to a conductive case with a higher T_b . Our two end-member temperature profiles thus capture the possible effects of temperature variations in the mantle of Mercury, under the assumption that there is no partial melting in the mantle.

To model the rheology of the mantle as a function of depth, we divided it into sublayers. Starting from the core-mantle boundary, we divided the mantle in 40-km-thick sublayers, as illustrated in Figure 3. For each sublayer the pressure and the temperature at the midpoint were calculated. The complex compliance for each sublayer was obtained with equations (5) and (6) of Section 2.1. The rigidity was calculated with equation (9). The viscosity is then given by the expression $\nu = 1/(J_I\omega)$. It is the viscosity of a Maxwell model with the same complex compliance, i.e., with the same rheology. The value of rigidity and viscosity so calculated were taken as representative of the full sublayer.

The Andrade rheological model has been successfully applied to the description of dissipation in rocks, ices, and metals (i.e., Efroimsky, 2012, and references therein). The model described in Section 2.1 currently represents the best available Andrade model parameterization that incorporates the effects of temperature, pressure, and grain size on the rheology. However the parameters that are kept fixed in the model (listed in Table 1) are based on laboratory data on olivine (Jackson *et al.*, 2010). In what follows we apply the Andrade model of Section 2.1 to different mineralogical models for the mantle of Mercury. We thus assume that the fixed parameters of olivine can be

Table 2: Minerals Relevant to the Mantle and Crust of Mercury

	Abbr.	ρ_0 kg/m ³	μ_0 GPa	$\mu'_P _0$	$\mu'_T _0$ GPa/K
Garnet	Grt	3565+760 χ_{Fe}	92+7 χ_{Fe}	1.4	-0.010
Orthopyroxene	Opx	3194+799 χ_{Fe}	78+10 χ_{Fe}	1.6	-0.012
Clinopyroxene	Cpx	3277+380 χ_{Fe}	67-6 χ_{Fe}	1.7	-0.010
Quartz	Qtz	2650	44.5	0.4	-0.001
Spinel	Spl	3580+700 χ_{Fe}	108-24 χ_{Fe}	0.5	-0.009
Plagioclase	Pl	2750	40.4	2.5	-0.002
Merwinite	Mw	3330	81	1.4	-0.014
Olivine	Ol	3222+1182 χ_{Fe}	81-31 χ_{Fe}	1.4	-0.014

Notes: Abbr. denotes mineral abbreviation (*Sivvola and Schmid, 2007*). A subscript “0” indicates standard ambient temperature and pressure (298 K, 10⁵ Pa). Density is ρ . μ , μ'_P , and μ'_T are the rigidity and its pressure and temperature derivatives, respectively. χ_{Fe} is the mole fraction of iron. Data in this table are taken from the compilations of *Sobolev and Babeyko (1994)*, *Vacher et al. (1998)*, *Cammarano et al. (2003)*, *Verhoeven et al. (2005)*, and *Rivoldini et al. (2009)*.

applied to other minerals. This assumption is not strictly correct, especially for mantle models in which olivine is not the dominant phase, but the broad applicability of the Andrade model to describe materials as chemically and physically different as ices and silicates indicates that the model we use should provide a good description of the rheology of silicate minerals.

4 Assessment of the Rheology of the Outer Solid Shell

The unrelaxed rigidity is a parameter required to characterize the rheology and thus the response to the tidal forcing. Different minerals have different rigidity values, so the mineral assemblages of the mantle and crust determine their rigidities. In this section we assess the impact of the composition on the rigidity of the mantle and the crust. Table 2 contains data for minerals that are be used below in modeling the rigidity of the mantle and crust of Mercury. In addition, we describe our assumptions in modeling the response of the FeS layer.

4.1 Mineralogical Models for the Mantle

For the mineralogy of the mantle, we use the works of *Rivoldini et al. (2009)* and *Malavergne et al. (2010)* as references. *Malavergne et al. (2010)* calculated the expected mineralogy of the mantle of Mercury as a function of pressure, given two different assumed bulk compositions for the whole planet, an enstatite chondrite (EH) and a Bencubbin-like chondrite (CB). The EH chondrite provides a good compositional and mineralogical match to the data of the X-Ray Spectrometer (XRS) on MESSENGER (*Weider et al., 2012*), which are compatible with the data from the Gamma-Ray Spectrometer (GRS) (*Evans et al., 2012*). The XRS and the GRS are sensitive to the

top tens of micrometers and centimeters of near-surface material, respectively, and the consistency between the results of the two instruments indicates that the top tens of centimeters of Mercury’s regolith are vertically homogeneous (*Evans et al.*, 2012). Despite the apparent good agreement between XRS and GRS results and enstatite chondrite compositions, the metal fraction in EH chondrites is lower than the bulk value for Mercury. The CB chondrites analyzed by *Malavergne et al.* (2010) have a higher metallic component, and thus might represent another possible building block for Mercury. *Rivoldini et al.* (2009) calculated the expected mineralogy for a set of five models of the mantle of Mercury. These included: an enstatite chondrite model (EC), similar to the EH case of *Malavergne et al.* (2010); a model in which the building blocks for Mercury are matched compositionally by the chondrules of two metal-rich chondrites (MC) (*Taylor and Scott*, 2005); a model based on fractionation processes in the solar nebula (MA) (*Morgan and Anders*, 1980); the refractory-volatile model (TS) of *Taylor and Scott* (2005); and the evaporation model of *Fegley and Cameron* (1987). The latter is not consistent with the high abundance of sulfur, potassium, and sodium in Mercury’s surface materials (*Nittler et al.*, 2011; *Peplowski et al.*, 2011; *Evans et al.*, 2012). We used the composition of these six models to estimate a range for the rigidity of the mantle of Mercury. The mineralogical composition of these models is listed in Table 3.

4.2 Rigidity of the Mantle

MESSENGER confirmed that the surface of Mercury has an extremely low iron abundance (*Nittler et al.*, 2011; *Evans et al.*, 2012) and showed that a substantial fraction of the surface is volcanic in origin (*Denevi et al.*, 2013). The low surface abundance of FeO is an indication that the source regions of volcanic material are also FeO poor, since FeO does not undergo major fractionation during partial melting (*Taylor and Scott*, 2005). However, under the highly reducing conditions inferred for Mercury, part of the iron in the silicate shell is present as sulfides and metal (*Zolotov et al.*, 2013). In calculating the rigidity of the mantle, we assume that the silicate minerals contain no iron. In other words we assume that $\chi_{\text{Fe}} = 0$ in Table 2. The effects of small amounts of iron-rich minerals are small compared with the uncertainties introduced by the unknown mineralogy of the mantle of Mercury. It should be noted, however, that at least for olivine the rheological properties show a strong dependence on the iron content (*Zhao et al.*, 2009).

For each mineralogical model of the mantle in Table 3 we calculate the composite rigidity at the reference conditions of $T_{\text{R}} = 1173$ K and $P_{\text{R}} = 0.2$ GPa, required for the Andrade model [equation (7)]. First, for each mineral the rigidity at T_{R} and P_{R} is obtained from the parameters in Table 2 with the expression

$$\mu_{\text{U}}(T_{\text{R}}, P_{\text{R}}) = \left[\mu_0 + (T - T_{\text{R}}) \frac{d\mu}{dT} + (P - P_{\text{R}}) \frac{d\mu}{dP} \right]. \quad (11)$$

The composite rigidity is obtained with Hill’s expression, which is an average between the Reuss and the Voigt rigidities (*Watt et al.*, 1976). Table 3 lists the composite rigidities so derived for the mantle models. The range is 59 – 71 GPa.

Table 3: Models for the Mantle of Mercury.

Model	Grt	Opx	Cpx	Qtz	Spl	Pl	Mw	Ol	μ_c (GPa)
CB	–	66	4	22	4	4	–	–	59
EH	–	78	2	8	–	12	–	–	65
MA	23	32	15	–	–	–	–	30	69
TS	25	–	–	–	8	–	2	65	71
MC	15	50	9	–	–	–	–	26	68
EC	1	75	7	17	–	–	–	–	60

Notes: Two capital letters identify the model (details in section 4.1). CB and EH: *Malavergne et al.* (2010). MA: *Morgan and Anders* (1980). TS and MC: *Taylor and Scott* (2005). EC: *Wasson* (1988). The central part of the table gives the mineralogical content in terms of the vol.% of its components (after *Malavergne et al.* (2010) and *Rivoldini et al.* (2009)). Mineral abbreviations are defined in Table 2. A dash indicates that the mineral is absent. The composite rigidity μ_c is evaluated as the Hill rigidity at $T = 1173$ K and $P = 0.2$ GPa.

Table 4: Composition and Rigidity of the Crust of Mercury.

Model	Ol	Opx	Pl	Spl	Qz	μ_c (GPa)
SP	2	44	26	6	22	53-58
SP _{Na}	8	30	57	5	–	51-53
IcP-HCT	2	59	29	1	9	57-60

Notes: “Model” column: SP stands for smooth plains, and IcP-HCT stands for intercrater plains and heavily cratered terrain. SP_{Na} takes into account the difference that might arise with a different Na abundance (see *Stockstill-Cahill et al.*, 2012). The central part of the table gives the mineralogical composition in weight percent. In the last column the composite rigidity is calculated with Hill’s expression. The range in μ_c for each model is given by the different amounts of end-members (i.e., forsterite and fayalite in the olivine solid-solution series).

4.3 Rigidity and Viscosity of the Crust

The surface of Mercury presents a compositional and morphological dichotomy between the younger smooth plains (SP) and the older intercrater plains and heavily cratered terrain (IcP-HCT) (*Peplowski et al.*, 2011; *Weider et al.*, 2012). The majority of the SP, which cover $\sim 27\%$ of the surface of Mercury, are volcanic in origin (*Denevi et al.*, 2013). From the surface compositional data returned by MESSENGER, *Stockstill-Cahill et al.* (2012) modeled the expected mineralogy of the IcP-HCT and the northern volcanic plains (NVP). The NVP are a large contiguous area of volcanic smooth plains (*Head et al.*, 2011) that show similar composition to other smooth plains (i.e., Caloris basin interior) (*Weider et al.*, 2012). Therefore the mineralogy of the NVP can be taken as representative of other smooth plains areas. The results of *Stockstill-Cahill et al.* (2012) are summarized in Table 4. The table also includes the mineralogy for smooth plains when the effect of uncertainties in the Na abundance are taken into account (SP_{Na}). These three mineralogies are used to estimate the rigidity of the crust of Mercury.

Variations in the temperature and pressure of the crust with depth have negligible effects on

the rigidities of the individual minerals. Therefore the composite rigidity is obtained with Hill’s expression using μ_0 (Table 2) as the rigidity for each mineral.

The range in crustal rigidity is 51 – 60 GPa, and will likely encompass the actual rigidity of the crust if the IcP-HCT represents the older crust and the SP are representative of the younger crust produced by the most recent widespread episodes of partial melting of the mantle. We use the central value of 55 GPa as the rigidity of the crust. Its viscosity is set at 10^{23} Pa s. This choice is not critical since the crust is cold and responds elastically at the forcing frequency of the tide.

4.4 Rheology of the FeS layer

The procedure used to calculate the rigidity of the mantle minerals cannot be used for the FeS layer because of a lack of laboratory data. At the relevant pressures and temperatures of the outer core of Mercury, the FeS would be in the FeS V phase (*Fei et al.*, 1995). For FeS V the bulk modulus and its pressure and temperature derivatives have been measured (*Urakawa et al.*, 2004). There is no rigidity determination, however. Even the rigidity of troilite (or FeS I, the phase at standard pressure and temperature) has never been measured (*Hofmeister and Mao*, 2003). Nevertheless, an argument illustrated by *Hofmeister and Mao* (2003, see their Figure 7) sets $\mu_{\text{FeS I}} = 31.5$ GPa. From the phase diagram of FeS (*Fei et al.*, 1995), the conditions at the base of the mantle ($P \sim 5.5$ GPa) are close to the melting curve for FeS V. The corresponding homologous temperature T_H , the ratio of the temperature of the material to the solidus temperature, is $T_H > 0.85$. It is often assumed that the viscosity is proportional to the exponential of the inverse of the homologous temperature (e.g., *Borch and Green II*, 1987). Therefore the viscosity of the FeS layer at the top of the core would be close to the low viscosity of the melt. These considerations indicate that the FeS layer, if present, is weak.

We consider the effects of the FeS layer only in the cold-mantle case ($T_b = 1600$ K), since for higher temperatures the FeS would be liquid (see the phase diagram in *Fei et al.*, 1995). We assume that the FeS will have the same rheological properties as the base of the mantle. This assumption is conservative because at $T = 1600$ K the T_H of FeS is larger than T_H of the silicates and, from the value of $\mu_{\text{FeS I}}$, the unrelaxed rigidity of FeS V is likely to be smaller than that for the silicates.

5 Results: Tidal Response and Interior Properties

The results illustrated below show that models of Mercury with a liquid outer core have $k_2 \gtrsim 0.3$. For a completely solid model of Mercury (i.e., a model devoid of a liquid outer core), the value of k_2 would be reduced by approximately an order of magnitude. Given this variation in the magnitude of k_2 between a completely solid interior and one with a liquid (outer) core, a measurement of the tidal response would provide a confirmation of the presence of a liquid (outer) core. Its existence has already been inferred from Earth-based radar measurements (*Margot et al.*, 2007) and also from the interpretation of the magnetic field detected by the MESSENGER Magnetometer (*Anderson et al.*, 2012). Therefore the results presented below focus on the models of Mercury with a liquid (outer) core that have been described in section 3.

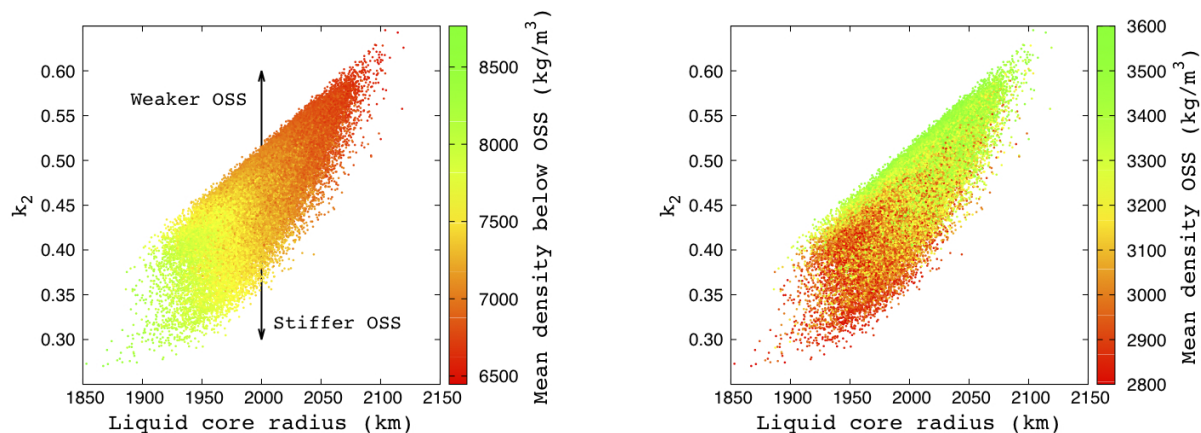


Figure 4: k_2 as a function of the radius of the liquid core for the NoFeS set. For these data the temperature at the base of the core is $T_b = 1725$ K and the mantle unrelaxed rigidity is $\mu_U = 65$ GPa. Left: Colors indicate the mean density of material below the outer solid shell (OSS). The arrows indicate how the data points would shift with a change in the rheological properties of the OSS. Right: Same as for the left panel, but here colors indicate the mean density of the OSS.

5.1 The Main Parameters Controlling the Tidal Deformation

The tidal response of Mercury is largely controlled by the strength and thickness of the outer solid shell (OSS), much like the similar case for Europa’s ice shell (*Moore and Schubert, 2000*). This result is a consequence of the presence of a liquid (outer) core, which decouples the shell from the deformation of the deeper interior. Due to the combined mass and moments of inertia constraints, the thickness of the OSS depends on the density of the core. This outcome is shown in the left panel of Figure 4, where the tradeoff between core density and liquid core radius (i.e., OSS thickness) is seen in the color scale that strongly correlates both with the radius of the liquid core and k_2 . For these models, $\mu_U = 65$ GPa and $T_b = 1725$ K. A modification of the rheological properties of the OSS, through a variation of the temperature at the base of the mantle T_b and/or of the unrelaxed rigidity μ_U , would modify the response as indicated by the arrows in the figure. Note, however, that there is only a weak dependence on the density of the OSS itself, as seen in the right panel of Figure 4, where the colors show the density of the OSS and span nearly the entire range of the response. The small effects of a solid inner core on the tidal response are discussed in Appendix A.

The same set of models used in Figure 4 are shown in Figure 5 in the form of a plot showing how the compatible models (section 3) are distributed. The availability for Mercury of the three constraints ρ , C , and C_m results in a distribution of the data that is relatively narrow, which makes the determination of k_2 in principle very useful. It has the potential for improving the determination of the location of the radius of the outer liquid core and the mean density of the material below the outer solid shell, and of providing insights into the rheological properties (temperature and rigidity) of the outer solid shell. This improved knowledge will depend both on the precision of the k_2 determination and on the effects of the uncertainties in the temperature and rigidity of the

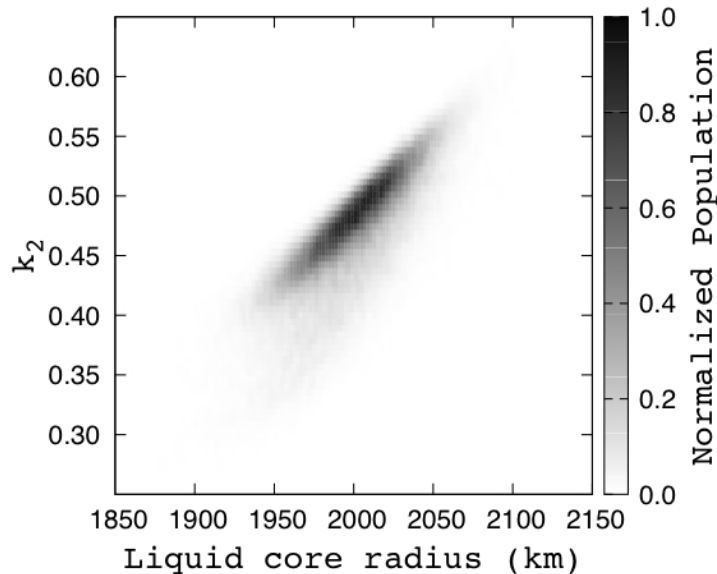


Figure 5: Same data as in Figure 4, here plotted using the normalized population based on the C and C_m determinations.

outer solid shell.

5.2 Effects of the Mantle Rheology on the Tidal Response

In our models the rheology of the outer shell is controlled by the temperature at the base of the mantle T_b and the unrelaxed rigidity of the mantle μ_U . Figure 6 illustrates the effects on the tidal response of a variation in T_b between 1600 K and 1850 K. For this case we assumed an unrelaxed mantle rigidity of $\mu_U = 65$ GPa. As expected, on the basis of the influence of temperature on rheology (Figure 1), a higher T_b corresponds to a weaker outer solid shell, which in turn has a larger tidal response. In terms of the central values of the model populations, k_2 varies in the range 0.47 – 0.50.

Basal mantle temperature and unrelaxed rigidity have similar, if opposite, effects on the tidal response, which is enhanced by a higher T_b and/or lower μ_U and is diminished by a lower T_b and/or higher μ_U . Therefore, there is a tradeoff between these two parameters. The full range of tidal responses for the NoFeS models is illustrated in Figure 7. The variation in k_2 is in the range 0.45 – 0.52, the former value corresponding to the stiff mantle ($T_b = 1600$ K and $\mu_U = 71$ GPa) and the latter to the weak mantle ($T_b = 1850$ K and $\mu_U = 59$ GPa). The values of μ_U that we use, 59 GPa and 71 GPa, represent the largest and smallest values derived from the mantle mineralogies analyzed in section 4.1 and listed in Table 3.

A solid FeS layer can exist only in the $T_b = 1600$ K case (Section 4.4). Under the assumptions for the rheology of solid FeS at the base of the mantle of Mercury described in Section 4.4, we

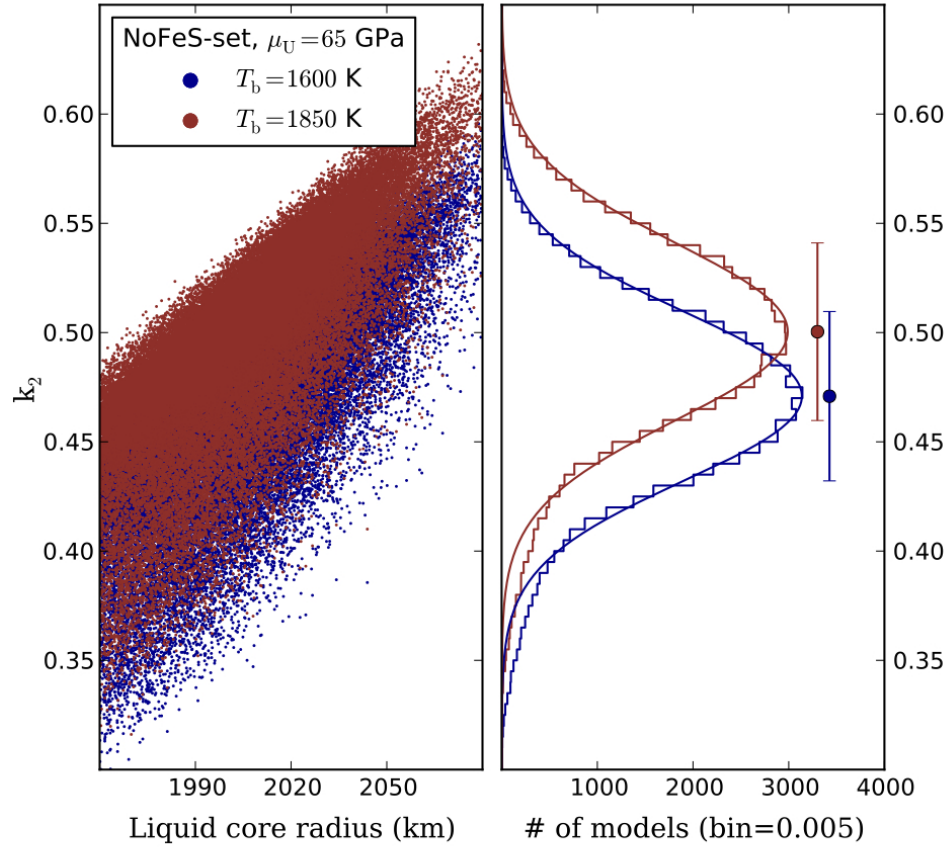


Figure 6: Effect of the mantle basal temperature on the tidal response. Predicted values of k_2 for models with unrelaxed rigidity $\mu_U = 65$ GPa and two different values of temperature at the base of the mantle $T_b = 1600$ K (dark blue) and $T_b = 1850$ K (brown). Left: k_2 as a function of the radius of the liquid core. Right: histogram of k_2 for the two sets of models.

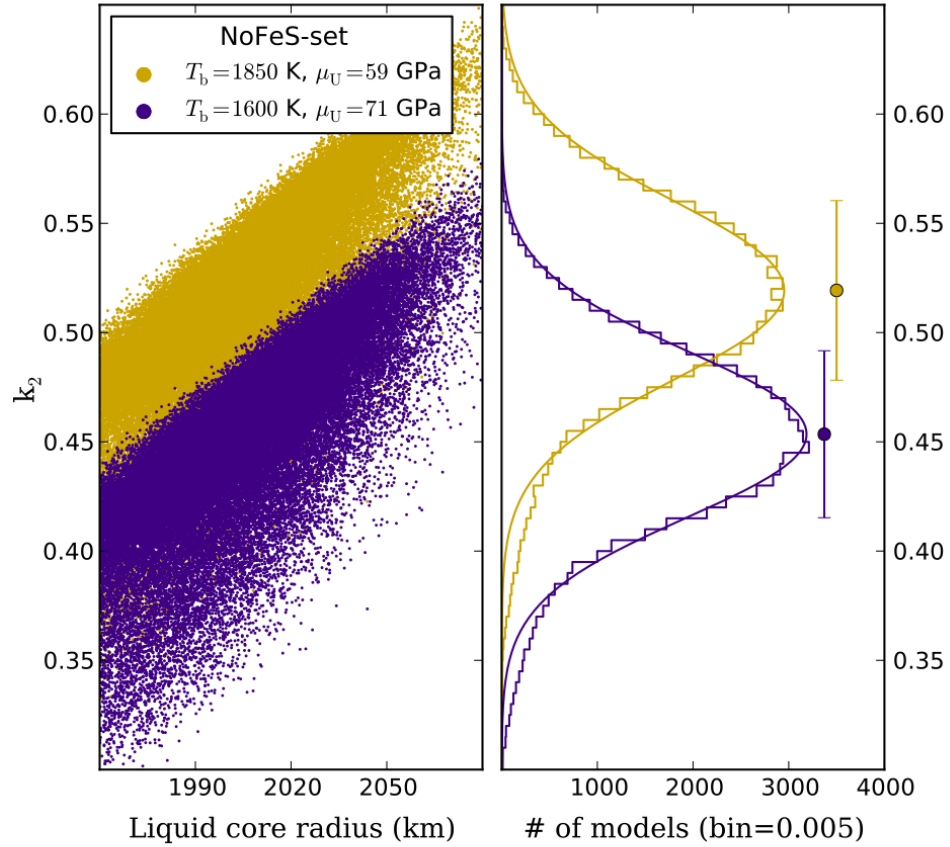


Figure 7: Predicted values of k_2 for the two end-member NoFeS sets of models. Golden: weak outer solid shell with mantle basal temperature $T_b = 1850$ K and unrelaxed rigidity $\mu_U = 59$ GPa. Indigo: stiff outer solid shell with $T_b = 1600$ K and $\mu_U = 71$ GPa. Left: k_2 as a function of the radius of the liquid core. Right: histogram of k_2 for the two sets of models.

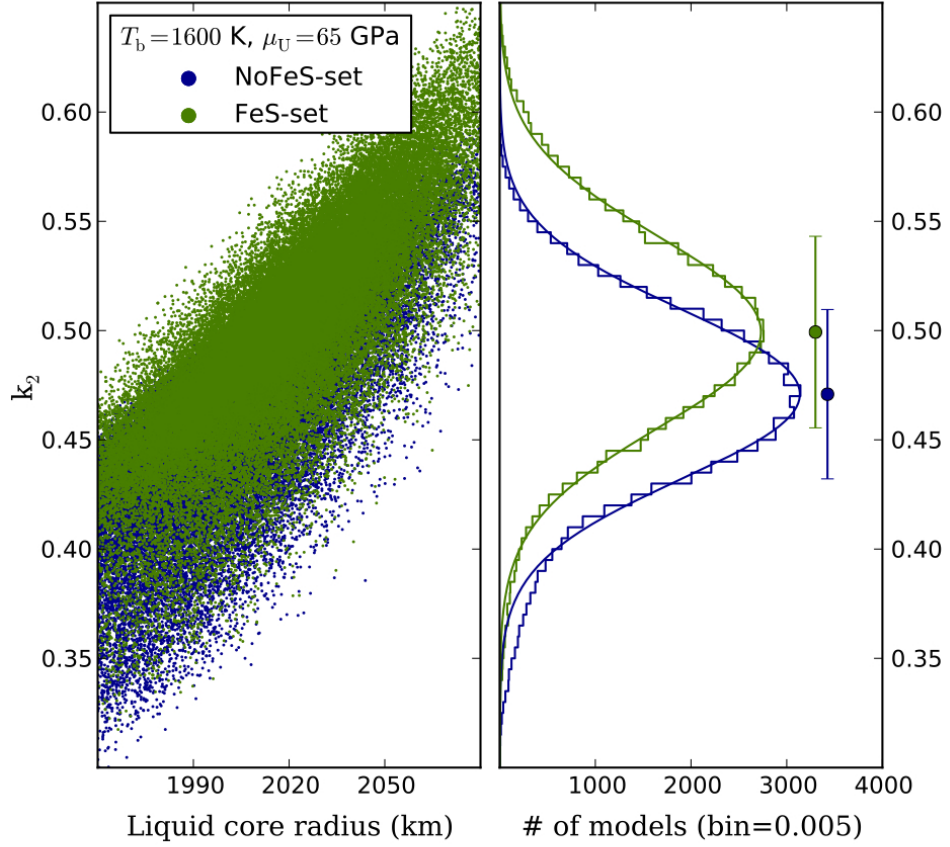


Figure 8: Effect of a solid FeS layer on the tidal response. Predicted values of k_2 for models with mantle basal temperature $T_b = 1600$ K and unrelaxed mantle rigidity $\mu_U = 65$ GPa, with (green) and without (dark blue) an FeS layer at the base of the mantle. Left: k_2 as a function of the radius of the liquid core. Right: histogram of k_2 for the two sets of models.

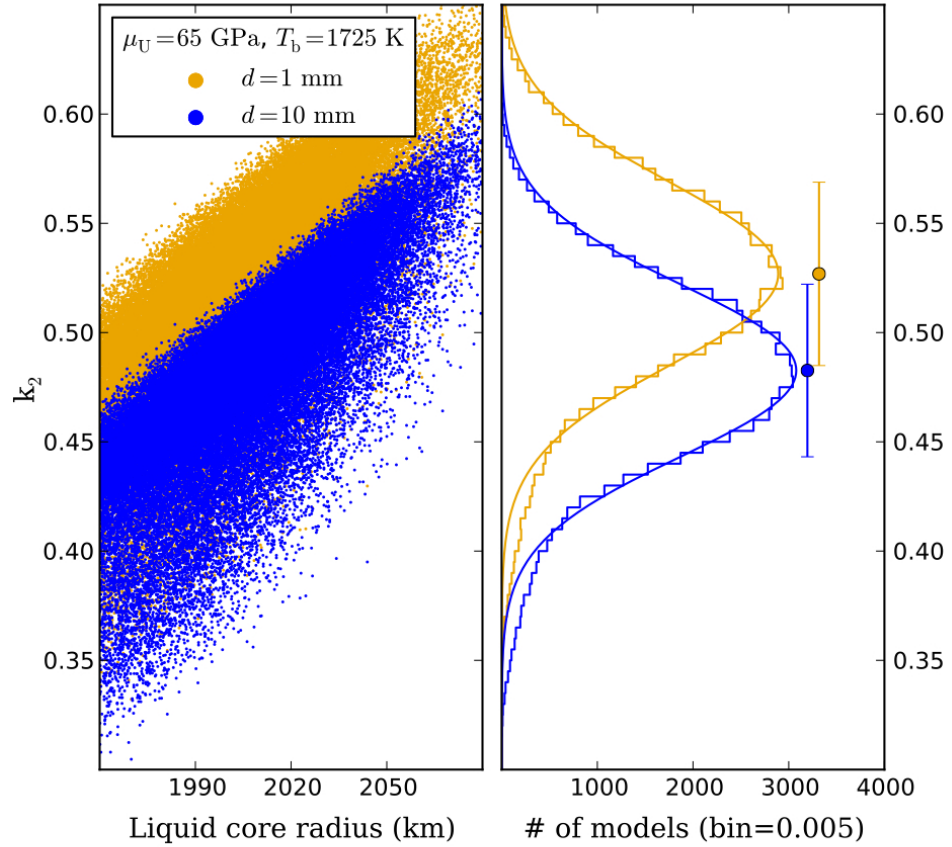


Figure 9: Predicted values of k_2 for two sets of NoFeS models with the same mantle basal temperature $T_b = 1725$ K and the same mantle unrelaxed rigidity $\mu_U = 59$ GPa. The two sets differ in the assumed mantle grain size d . Blue: $d = 1$ cm. Orange: $d = 1$ mm. Left: k_2 as a function of the radius of the liquid core. Right: histogram of k_2 for the two sets of models.

tested for the effect of the presence of an FeS layer on the tidal response for the case of $T_b = 1600$ K. Results are shown in Figure 8. The effect of the weak FeS layer is to increase the tidal response. In other words, it has the same effect as a higher T_b or a lower μ_U . In terms of the central k_2 values of the model populations, the presence of the FeS layer increases the tidal response by $\sim 6\%$.

The models presented are for a mantle grain size $d = 1$ cm. A smaller grain size, $d = 1$ mm, corresponds to a more dissipative rheology, which induces a larger tidal response. This effect is illustrated in Figure 9. The effect is substantial, since in this case k_2 varies between 0.48 and 0.52, a larger range than the one resulting from the variation of T_b illustrated in Figure 6.

6 Summary and Conclusions

We performed simulations of the tidal response of Mercury, as parameterized by the tidal Love number k_2 , for two sets of models of Mercury that are compatible with the currently available constraints on the interior structure of the planet, i.e., the mean density ρ , the moment of inertia C , and the moment of inertia of the outer solid shell C_m . The two sets of models differ in the presence or absence of a solid FeS layer at the top of the core (section 3). The response of the materials is modeled with viscoelastic rheologies (section 2.1). The Maxwell rheological model is used for the crust, the liquid outer core, and the solid inner core. The Andrade rheological model is used for the mantle, where the high temperature and relatively low pressure induce large non-elastic effects (Figure 1 and Table 1). For the FeS layer we assumed an Andrade rheology that matches the basal mantle layer. We investigated the effects on the tidal response of the unknown mantle mineralogy (which determines the unrelaxed rigidity μ_U), temperature profile in the outer solid shell (controlled by the mantle basal temperature T_b), and mantle grain size.

The main findings of the paper can be summarized as follows:

1. The presence of a liquid outer core makes the value of k_2 dependent mainly on three parameters: the radius of the liquid core (Figure 5), the mean density of material below the outer solid shell (Figure 4, left panel), and the rheology of the outer solid shell (Figures 6 to 9). Since the first two have been determined with a precision of better than 5% from ρ , C , and C_m (Hauck *et al.*, 2013; Rivoldini and Van Hoolst, 2013), a measurement of k_2 is informative with regard to the rheology of the outer solid shell;
2. With available estimates for the temperature at the base of the mantle T_b (Rivoldini and Van Hoolst, 2013; Tosi *et al.*, 2013), for an unrelaxed rigidity μ_U of the mantle appropriate for mineralogical models compatible with MESSENGER observations (Table 3), and with a mantle grain size $d = 1$ cm, we find that for the NoFeS-set k_2 varies in the range 0.45 – 0.52. This range is expressed in terms of the central values of the model populations shown in the right panel of Figure 7 and corresponds to models with $(T_b, \mu_U) = (1600 \text{ K}, 71 \text{ GPa})$ and $(T_b, \mu_U) = (1850 \text{ K}, 59 \text{ GPa})$, respectively. An order of magnitude reduction in the grain size would result in a $\gtrsim 10\%$ increase in the tidal response (Figure 9);
3. The presence of a solid FeS layer is possible only if $T_b \lesssim 1600$ K (Section 4.4). Its effect is to increase the tidal response by $\sim 6\%$ (Figure 8). This result is obtained under the

conservative assumption that the FeS layer has the same rheological properties as the base of the mantle (Section 4.4). The solid FeS may be weaker, in which case its effect would be larger than the estimate shown in Figure 8.

The possibility of improving our understanding of the interior of Mercury through the interpretation of a measurement of k_2 depends on the precision of the determination obtained by the radio tracking of the MESSENGER spacecraft (or BepiColombo in the future), and on the uncertainties in the parameters that affect the tidal response of the planet.

As mentioned in section 2, the highly eccentric orbit of MESSENGER makes the determination of k_2 very challenging. Nevertheless, there are indications that the solution will converge to a value of $\sim 0.45 \pm 0.05$ (Mazarico *et al.*, 2014). If confirmed, such a result would fall in the lower range of our model responses. With the preliminary estimate of $k_2 = 0.45$, Figures 6 to 8 suggest that a cold mantle model, without an FeS layer, is preferred. For the results presented in these figures a mantle grain size $d = 1$ cm was assumed, a value compatible with the estimated grain size for the mantles of the Moon and Mars (Nimmo *et al.*, 2012; Nimmo and Faul, 2013). A smaller grain size would result in an increased tidal deformation (Figure 9) and would strengthen the preference for a cold mantle model, without and FeS layer. Nevertheless, the uncertainties associated both with the k_2 determination and with the modeled distributions are too large to make a conclusive statement.

Future improvements in the interpretation of k_2 can be expected. Our modeling of the tidal response would benefit from improvements in the mineralogical models of the silicate part (which would reduce the range in the unrelaxed rigidity μ_U). No meteorites from Mercury have yet been identified, and there are currently no plans for a lander or sample return mission to Mercury, so improvements in compositional models will be based on additional remote sensing measurements, cosmochemical analogues, experimental petrological observations (e.g., McCoy *et al.*, 1999; Charlier *et al.*, 2013), and numerical simulations (e.g., Stockstill-Cahill *et al.*, 2012). Updates in the estimates of the amount of global contraction of Mercury will inform thermal history models, which in turn put constraints on the basal mantle temperature (e.g., Tosi *et al.*, 2013).

A Effect of the Inner Core on the Tidal Response

The effect of the inner core density on the magnitude of k_2 is shown in Figure 10. The relatively weak trend indicates that the Love number k_2 is not very sensitive to the density of the inner core. A similar plot for k_2 as a function of the ratio of the inner core radius, r_{ic} , to the radius of the outer core, r_{oc} , is shown in the bottom panel of Figure 11. The results show that k_2 is independent of the ratio of inner-core radius to outer-core radius as long as the inner core is sufficiently small. The lack of shear strength of the liquid of the outer core increases the tidal response and makes it independent of the size of the inner core, as long as the radius ratio is $\lesssim 0.6$.

Similarly, variations in the viscosity and rigidity of the inner core affect the value of k_2 only for those models that have a large inner core. Less than 20% of the models have a large inner core with $r_{ic}/r_{oc} > 0.6$ as shown by the cumulative histogram in the top panel of Figure 11. A very large inner core may be detectable, because it would modify the libration of Mercury (?) at a level

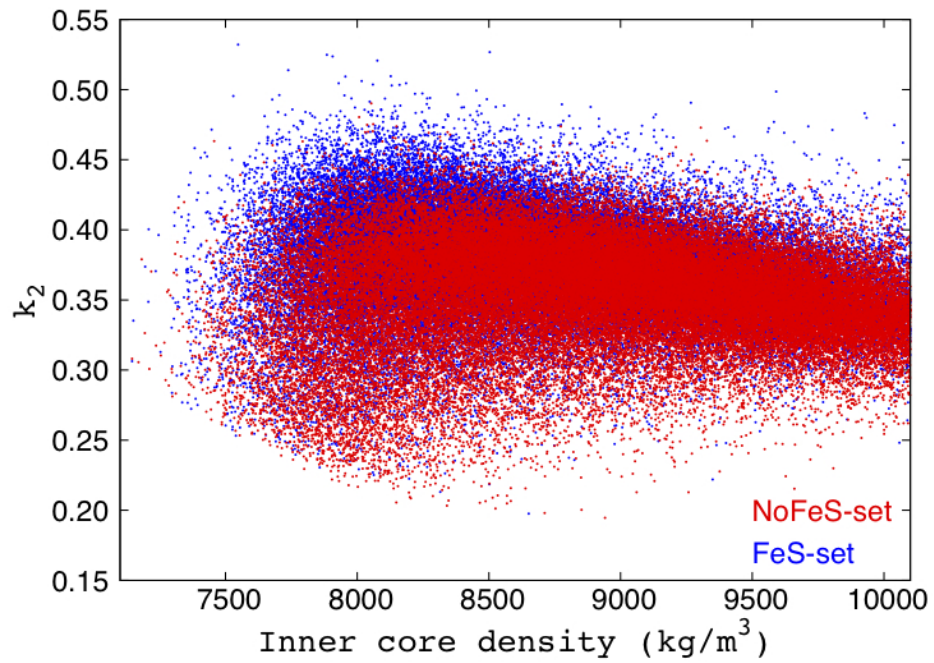


Figure 10: k_2 as a function of the inner core density. Blue and red points correspond to models with and without an FeS layer at the top of the core, respectively.

that is comparable to the current observational accuracy of the libration measurements (*Margot et al.*, 2012).

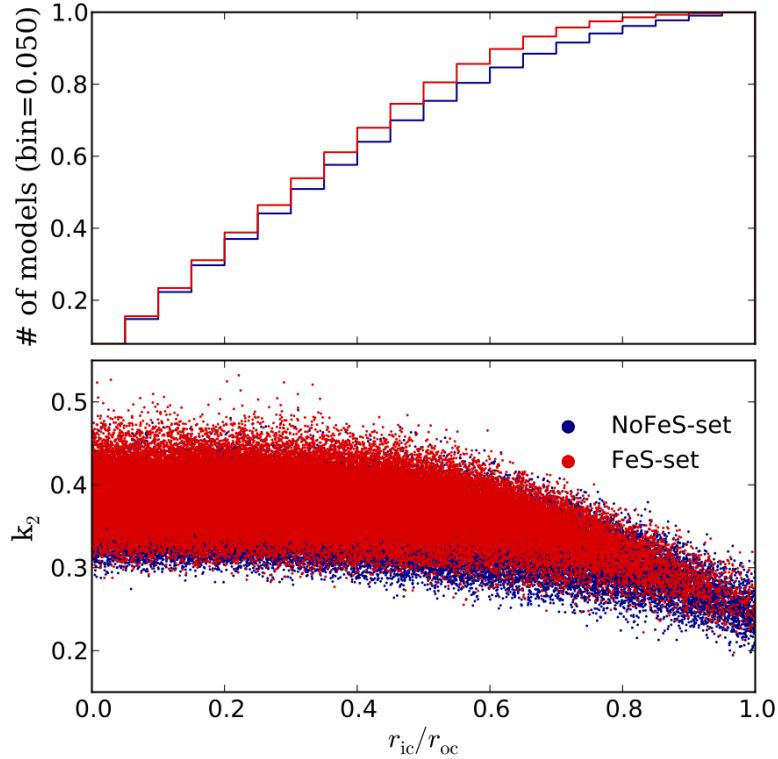


Figure 11: (Top) Cumulative histogram of the ratio of the inner core radius r_{ic} to the liquid outer core radius r_{oc} . More than 80% of the models have $r_{ic}/r_{oc} < 0.6$. (Bottom) k_2 as a function of the inner core radius expressed in units of outer core radius. Blue and red points correspond to models with and without an FeS layer at the top of the core, respectively. Points with an abscissa close to one correspond to models for which the outer liquid core is very thin. Models in which the core is completely solid have k_2 values that are smaller by approximately an order of magnitude (not shown).

References

- Alterman, Z., H. Jarosch, and C. L. Pekeris (1959), Oscillations of the Earth, *Proc. Roy. Soc. Lond., Ser. A*, *252*, 80–95, doi:10.1098/rspa.1959.0138.
- Anderson, B. J., C. L. Johnson, H. Korth, R. M. Winslow, J. E. Borovsky, M. E. Purucker, J. A. Slavin, S. C. Solomon, M. T. Zuber, and R. L. McNutt Jr. (2012), Low-degree structure in Mercury’s planetary magnetic field, *J. Geophys. Res.*, *117*, E00L12, doi:10.1029/2012JE004159.
- Arfken, G. B., and H. J. Weber (2005), *Mathematical Methods for Physicists: A Comprehensive Guide*, 6th ed., Academic Press.
- Biot, M. A. (1954), Theory of stress-strain relations in anisotropic viscoelasticity and relaxation phenomena, *J. Appl. Phys.*, *25*, 1385–1391, doi:10.1063/1.1721573.
- Borch, R. S., and H. W. Green II (1987), Dependence of creep in olivine on homologous temperature and its implications for flow in the mantle, *Nature*, *330*, 345–348, doi:10.1038/330345a0.
- Cammarano, F., S. Goes, P. Vacher, and D. Giardini (2003), Inferring upper-mantle temperatures from seismic velocities, *Phys. Earth Planet. Inter.*, *138*, 197–222, doi:10.1016/S0031-9201(03)00156-0.
- Charlier, B., T. L. Grove, and M. T. Zuber (2013), Phase equilibria of ultramafic compositions on Mercury and the origin of the compositional dichotomy, *Earth Planet. Sci. Lett.*, *363*, 50–60, doi:10.1016/j.epsl.2012.12.021.
- Christensen, U. R. (2006), A deep dynamo generating Mercury’s magnetic field, *Nature*, *444*, 1056–1058, doi:10.1038/nature05342.
- Colombo, G. (1966), Cassini’s second and third laws, *Astron. J.*, *71*, 891–896, doi:10.1086/109983.
- Denevi, B. W., C. M. Ernst, H. M. Meyer, M. S. Robinson, S. L. Murchie, J. L. Whitten, J. W. Head, T. R. Watters, S. C. Solomon, L. R. Ostrach, C. R. Chapman, P. K. Byrne, C. Klimczak, and P. N. Peplowski (2013), The distribution and origin of smooth plains on Mercury, *J. Geophys. Res. Planets*, *118*, 891–907, doi:10.1002/jgre.20075.
- Efroimsky, M. (2012), Bodily tides near spin-orbit resonances, *Celestial Mechanics and Dynamical Astronomy*, *112*, 283–330, doi:10.1007/s10569-011-9397-4.
- Efroimsky, M., and V. Lainey (2007), Physics of bodily tides in terrestrial planets and the appropriate scales of dynamical evolution, *J. Geophys. Res.*, *112*, E12003, doi:10.1029/2007JE002908.
- Evans, L. G., P. N. Peplowski, E. A. Rhodes, D. J. Lawrence, T. J. McCoy, L. R. Nittler, S. C. Solomon, A. L. Sprague, K. R. Stockstill-Cahill, R. D. Starr, S. Z. Weider, W. V. Boynton, D. K. Hamara, and J. O. Goldsten (2012), Major-element abundances on the surface of Mercury: Results from the MESSENGER Gamma-Ray Spectrometer, *J. Geophys. Res.*, *117*, E00L07, doi:10.1029/2012JE004178.

- Fegley, B., and A. G. W. Cameron (1987), A vaporization model for iron/silicate fractionation in the Mercury protoplanet, *Earth Planet. Sci. Lett.*, *82*, 207–222, doi:10.1016/0012-821X(87)90196-8.
- Fei, Y., C. T. Prewitt, H.-K. Mao, and C. M. Bertka (1995), Structure and density of FeS at high pressure and high temperature and the internal structure of Mars, *Science*, *268*, 1892–1894, doi:10.1126/science.268.5219.1892.
- Hauck, S. A., II, J.-L. Margot, S. C. Solomon, R. J. Phillips, C. L. Johnson, F. G. Lemoine, E. Mazarico, T. J. McCoy, S. Padovan, S. J. Peale, M. E. Perry, D. E. Smith, and M. T. Zuber (2013), The curious case of Mercury’s internal structure, *J. Geophys. Res. Planets*, *118*, 1204–1220, doi:10.1002/jgre.20091.
- Head, J. W., C. R. Chapman, R. G. Strom, C. I. Fassett, B. W. Denevi, D. T. Blewett, C. M. Ernst, T. R. Watters, S. C. Solomon, S. L. Murchie, L. M. Prockter, N. L. Chabot, J. J. Gillis-Davis, J. L. Whitten, T. A. Goudge, D. M. H. Baker, D. M. Hurwitz, L. R. Ostrach, Z. Xiao, W. J. Merline, L. Kerber, J. L. Dickson, J. Oberst, P. K. Byrne, C. Klimczak, and L. R. Nittler (2011), Flood volcanism in the northern high latitudes of Mercury revealed by MESSENGER, *Science*, *333*, 1853–1856, doi:10.1126/science.1211997.
- Hirschmann, M. M. (2000), Mantle solidus: Experimental constraints and the effects of peridotite composition, *Geochem. Geophys. Geosyst.*, *1*, 1042–1068, doi:10.1029/2000GC000070.
- Hofmeister, A., and H. Mao (2003), Pressure derivatives of shear and bulk moduli from the thermal Gruneisen parameter and volume-pressure data, *Geochim. Cosmochim. Acta*, *67*, 1207–1227, doi:10.1016/S0016-7037(02)01289-9.
- Iess, L., R. A. Jacobson, M. Ducci, D. J. Stevenson, J. I. Lunine, J. W. Armstrong, S. W. Asmar, P. Racioppa, N. J. Rappaport, and P. Tortora (2012), The tides of Titan, *Science*, *337*, 457–459, doi:10.1126/science.1219631.
- Jackson, I., U. H. Faul, D. Suetsugu, C. Bina, T. Inoue, and M. Jellinek (2010), Grainsize-sensitive viscoelastic relaxation in olivine: Towards a robust laboratory-based model for seismological application, *Phys. Earth Planet. Inter.*, *183*, 151–163, doi:10.1016/j.pepi.2010.09.005.
- Konopliv, A. S., and C. F. Yoder (1996), Venusian k_2 tidal Love number from Magellan and PVO tracking data, *Geophys. Res. Lett.*, *23*, 1857–1860.
- Konopliv, A. S., S. W. Asmar, W. M. Folkner, Ö. Karatekin, D. C. Nunes, S. E. Smrekar, C. F. Yoder, and M. T. Zuber (2011), Mars high resolution gravity fields from MRO, Mars seasonal gravity, and other dynamical parameters, *Icarus*, *211*, 401–428, doi:10.1016/j.icarus.2010.10.004.
- Konopliv, A. S., R. S. Park, D.-N. Yuan, S. W. Asmar, M. M. Watkins, J. G. Williams, E. Fahnestock, G. Kruiyinga, M. Paik, D. Strelakov, N. Harvey, D. E. Smith, and M. T. Zuber (2013), The JPL lunar gravity field to spherical harmonic degree 660 from the GRAIL Primary Mission, *J. Geophys. Res. Planets*, *118*, 1415–1434, doi:10.1002/jgre.20097.

- Lemoine, F. G., S. Goossens, T. J. Sabaka, J. B. Nicholas, E. Mazarico, D. D. Rowlands, B. D. Loomis, D. S. Chinn, D. S. Caprette, G. A. Neumann, D. E. Smith, and M. T. Zuber (2013), High-degree gravity models from GRAIL primary mission data, *J. Geophys. Res. Planets*, *118*, 1676–1698, doi:10.1002/jgre.20118.
- Malavergne, V., M. J. Toplis, S. Berthet, and J. Jones (2010), Highly reducing conditions during core formation on Mercury: Implications for internal structure and the origin of a magnetic field, *Icarus*, *206*, 199–209, doi:10.1016/j.icarus.2009.09.001.
- Margot, J.-L., S. J. Peale, R. F. Jurgens, M. A. Slade, and I. V. Holin (2007), Large longitude libration of Mercury reveals a molten core, *Science*, *316*, 710–714, doi:10.1126/science.1140514.
- Margot, J.-L., S. J. Peale, S. C. Solomon, S. A. Hauck II, F. D. Ghigo, R. F. Jurgens, M. Yseboodt, J. D. Giorgini, S. Padovan, and D. B. Campbell (2012), Mercury’s moment of inertia from spin and gravity data, *J. Geophys. Res.*, *117*, E00L09, doi:10.1029/2012JE004161.
- Mazarico, E., A. Genova, S. J. Goossens, F. G. Lemoine, D. E. Smith, M. T. Zuber, G. A. Neumann, and S. C. Solomon (2014), The gravity field of Mercury from MESSENGER, *Lunar Planet. Sci.*, *45*, abstract 1863.
- McCoy, T. J., T. L. Dickinson, and G. E. Lofgren (1999), Partial melting of the Indarch (EH4) meteorite: A textural, chemical and phase relations view of melting and melt migration, *Meteorit. Planet. Sci.*, *34*, 735–746, doi:10.1111/j.1945-5100.1999.tb01386.x.
- Michel, N. C., S. A. Hauck II, S. C. Solomon, R. J. Phillips, J. H. Roberts, and M. T. Zuber (2013), Thermal evolution of Mercury as constrained by MESSENGER observations, *J. Geophys. Res. Planets*, *118*, 1033–1044, doi:10.1002/jgre.20049.
- Milani, A., A. Rossi, D. Vokrouhlický, D. Villani, and C. Bonanno (2001), Gravity field and rotation state of Mercury from the BepiColombo Radio Science Experiments, *Planet. Space Sci.*, *49*, 1579–1596, doi:10.1016/S0032-0633(01)00095-2.
- Moore, W. B., and G. Schubert (2000), Note: The tidal response of Europa, *Icarus*, *147*, 317–319, doi:10.1006/icar.2000.6460.
- Morgan, J. W., and E. Anders (1980), Chemical composition of Earth, Venus, and Mercury, *Proc. Nat. Acad. Sci.*, *77*, 6973–6977, doi:10.1073/pnas.77.12.6973.
- Murray, C. D., and S. F. Dermott (1999), *Solar System Dynamics*, Cambridge University Press.
- Nimmo, F., and U. H. Faul (2013), Dissipation at tidal and seismic frequencies in a melt-free, anhydrous Mars, *J. Geophys. Res. Planets*, *118*, 2558–2569, doi:10.1002/2013JE004499.
- Nimmo, F., U. H. Faul, and E. J. Garnero (2012), Dissipation at tidal and seismic frequencies in a melt-free Moon, *J. Geophys. Res.*, *117*, E09005, doi:10.1029/2012JE004160.

- Nittler, L. R., R. D. Starr, S. Z. Weider, T. J. McCoy, W. V. Boynton, D. S. Ebel, C. M. Ernst, L. G. Evans, J. O. Goldsten, D. K. Hamara, D. J. Lawrence, R. L. McNutt Jr., C. E. Schlemm, S. C. Solomon, and A. L. Sprague (2011), The major-element composition of Mercury’s surface from MESSENGER X-ray spectrometry, *Science*, *333*, 1847–1850, doi:10.1126/science.1211567.
- Peale, S. J. (1969), Generalized Cassini’s laws, *Astron. J.*, *74*, 483–489, doi:10.1086/110825.
- Peale, S. J. (1976), Does Mercury have a molten core?, *Nature*, *262*, 765–766, doi:10.1038/262765a0.
- Peplowski, P. N., L. G. Evans, S. A. Hauck II, T. J. McCoy, W. V. Boynton, J. J. Gillis-Davis, D. S. Ebel, J. O. Goldsten, D. K. Hamara, D. J. Lawrence, R. L. McNutt Jr., L. R. Nittler, S. C. Solomon, E. A. Rhodes, A. L. Sprague, R. D. Starr, and K. R. Stockstill-Cahill (2011), Radioactive elements on Mercury’s surface from MESSENGER: Implications for the planet’s formation and evolution, *Science*, *333*, 1850–1852, doi:10.1126/science.1211576.
- Rivoldini, A., and T. Van Hoolst (2013), The interior structure of Mercury constrained by the low-degree gravity field and the rotation of Mercury, *Earth Planet. Sci. Lett.*, *377*, 62–72, doi:10.1016/j.epsl.2013.07.021.
- Rivoldini, A., T. van Hoolst, and O. Verhoeven (2009), The interior structure of Mercury and its core sulfur content, *Icarus*, *201*, 12–30, doi:10.1016/j.icarus.2008.12.020.
- Siivola, J., and R. Schmid (2007), List of mineral abbreviations, Recommendations by the IUGS Subcommittee on the Systematics of Metamorphic Rocks, *Electronic Source*: http://www.bgs.ac.uk/scmr/docs/papers/paper_12.pdf.
- Smith, D. E., M. T. Zuber, R. J. Phillips, S. C. Solomon, S. A. Hauck II, F. G. Lemoine, E. Mazarico, G. A. Neumann, S. J. Peale, J.-L. Margot, C. L. Johnson, M. H. Torrence, M. E. Perry, D. D. Rowlands, S. Goossens, J. W. Head, and A. H. Taylor (2012), Gravity field and internal structure of Mercury from MESSENGER, *Science*, *336*, 214–217, doi:10.1126/science.1218809.
- Sobolev, S. V., and A. Y. Babeyko (1994), Modeling of mineralogical composition, density and elastic wave velocities in anhydrous magmatic rocks, *Surv. Geophys.*, *15*, 515–544, doi:10.1007/BF00690173.
- Stockstill-Cahill, K. R., T. J. McCoy, L. R. Nittler, S. Z. Weider, and S. A. Hauck II (2012), Magnesium-rich crustal compositions on Mercury: Implications for magmatism from petrologic modeling, *J. Geophys. Res.*, *117*, E00L15, doi:10.1029/2012JE004140.
- Taylor, G. J., and E. R. D. Scott (2005), Mercury, in *Meteorites, Comets and Planets*, edited by A. M. Davis, in *Treatise on Geochemistry, Vol. 1.*, edited by H. D. Holland and K. K. Turekian, pp. 477–485, Elsevier, Amsterdam, The Netherlands, doi:10.1016/B0-08-043751-6/01071-9.
- Tosi, N., M. Grott, A.-C. Plesa, and D. Breuer (2013), Thermochemical evolution of Mercury’s interior, *J. Geophys. Res. Planets*, *118*, 2474–2487, doi:10.1002/jgre.20168.

- Turcotte, D. L., and G. Schubert (2002), *Geodynamics*, 2nd ed., Cambridge University Press, doi:10.2277/0521661862.
- Urakawa, S., K. Someya, H. Terasaki, T. Katsura, S. Yokoshi, K.-I. Funakoshi, W. Utsumi, Y. Katayama, Y.-I. Sueda, and T. Irifune (2004), Phase relationships and equations of state for FeS at high pressures and temperatures and implications for the internal structure of Mars, *Phys. Earth Planet. Inter.*, *143*, 469–479, doi:10.1016/j.pepi.2003.12.015.
- Vacher, P., A. Mocquet, and C. Sotin (1998), Computation of seismic profiles from mineral physics: The importance of the non-olivine components for explaining the 660 km depth discontinuity, *Phys. Earth Planet. Inter.*, *106*, 277–300.
- Van Hoolst, T., and C. Jacobs (2003), Mercury’s tides and interior structure, *J. Geophys. Res.*, *108*, 5121, doi:10.1029/2003JE002126.
- Verhoeven, O., A. Rivoldini, P. Vacher, A. Mocquet, G. Choblet, M. Menvielle, V. Dehant, T. Van Hoolst, J. Sleewaegen, J.-P. Barriot, and P. Lognonné (2005), Interior structure of terrestrial planets: Modeling Mars’ mantle and its electromagnetic, geodetic, and seismic properties, *J. Geophys. Res.*, *110*, E04009, doi:10.1029/2004JE002271.
- Wasson, J. T. (1988), The building stones of the planets, in *Mercury*, edited by F. Vilas, C. R. Chapman, and M. S. Matthews, pp. 622–650, University of Arizona Press, Tucson, Ariz.
- Watt, J. P., G. F. Davies, and R. J. O’Connell (1976), The elastic properties of composite materials, *Rev. Geophys. Space Phys.*, *14*, 541–563, doi:10.1029/RG014i004p00541.
- Weider, S. Z., L. R. Nittler, R. D. Starr, T. J. McCoy, K. R. Stockstill-Cahill, P. K. Byrne, B. W. Denevi, J. W. Head, and S. C. Solomon (2012), Chemical heterogeneity on Mercury’s surface revealed by the MESSENGER X-Ray Spectrometer, *J. Geophys. Res.*, *117*, E00L05, doi:10.1029/2012JE004153.
- Wolf, D. (1994), Lamé’s problem of gravitational viscoelasticity: The isochemical, incompressible planet, *Geophys. J. Int.*, *116*, 321–348, doi:10.1111/j.1365-246X.1994.tb01801.x.
- Yoder, C. F., A. S. Konopliv, D. N. Yuan, E. M. Standish, and W. M. Folkner (2003), Fluid core size of Mars from detection of the solar tide, *Science*, *300*, 299–303, doi:10.1126/science.1079645.
- Zhao, Y.-H., M. E. Zimmerman, and D. L. Kohlstedt (2009), Effect of iron content on the creep behavior of olivine: 1. Anhydrous conditions, *Earth Planet. Sci. Lett.*, *287*, 229–240, doi:10.1016/j.epsl.2009.08.006.
- Zolotov, M. Y., A. L. Sprague, S. A. Hauck II, L. R. Nittler, S. C. Solomon, and S. Z. Weider (2013), The redox state, FeO content, and origin of sulfur-rich magmas on Mercury, *J. Geophys. Res. Planets*, *118*, 138–146, doi:10.1029/2012JE004274.
- Zuber, M. T., D. E. Smith, D. H. Lehman, T. L. Hoffman, S. W. Asmar, and M. M. Watkins (2013), Gravity Recovery and Interior Laboratory (GRAIL): Mapping the lunar interior from crust to core, *Space Sci. Rev.*, *178*, 3–24, doi:10.1007/s11214-012-9952-7.